International Journal of Hydrogen Energy 58 (2024) 79–92

Contents lists available at ScienceDirect

International Journal of Hydrogen Energy

journal homepage: www.elsevier.com/locate/he

Hydrogen adsorption on Ni-functionalized saponites and their precursor gel

L. Masci [a,*], L. Truche [a], V. Magnin [a], M. Lanson [a], P. De Rango [b], A. Moya [a], N. Findling [a], B. Lanson [a], A. Viola [c], J. Deseure [c], M. Abdel Sater [d], P. Launois [d], G. Joubert [e], H. Toubon [e]

[a] Univ. Grenoble Alpes, Univ. Savoie Mont Blanc, CNRS, IRD, Univ. Gustave Eiffel, ISTerre, 38000, Grenoble, France
[b] Univ. Grenoble Alpes, CNRS, Institut Néel, 38000, Grenoble, France
[c] University Grenoble Alpes, University Savoie Mont Blanc, CNRS, Grenoble INP (Institute of Engineering and Management University Grenoble Alpes), LEPMI, 38000, Grenoble, France
[d] Laboratoire de Physique des Solides, CNRS, Université Paris-Saclay, F-91405, Orsay, France
[e] ORANO, 125 Av. de Paris, 92320, Châtillon, France

ARTICLE INFO

Handling Editor: Dr A Bhatnagar

Keywords:
Clay materials
Saponite
H_2 adsorption
Isotherms
Specific surface area
Ni functionalization
Hydrogen storage

ABSTRACT

Here we propose to investigate Ni-functionalized saponite (smectite group) as a viable alternative for low cost H_2 storage for land-based applications. The precursor gel used for saponite synthesis is also tested with respect to its H_2 adsorption properties. Adsorption isotherms recorded at 77 K and 1 bar, 298 K and 120 bar indicate that nickel functionalization does not induce a clear structural or chemical control on the adsorption process. However, Ni-pillared saponites outgassed at 70 °C display a four-time enhanced H_2 uptake (up to 0.12 wt% at 77 K and 1 bar) compared to its counterpart outgassed at 150 °C. Another important finding of this study is the surprisingly high H_2 uptakes of the gel (nano-crystallized) precursor, used for the synthesis of saponite samples (up to 0.19 wt% at 77 K and 1 bar, and up to 0.12 wt% at 298 K and 120 bar).

1. Introduction

This last decade has seen an increase of interest for hydrogen (H_2) as a carbon free energy vector that can be stored [1–4]. If produced by water electrolysis from renewable energy, or from fossil fuels with carbon capture and sequestration, this molecule is a good candidate to replace fossil fuels, for both mobile and stationary applications, because of its high energy density per mass unit (142 MJ/kg) [1,3,5]. However, one of hydrogen main drawbacks lies in its low volumetric density at ambient temperature and pressure, which requires specific storage technologies. Besides conventional storage methods such as high-pressure gas reservoirs (up to 700 bar at ambient temperature), cryo-compression (supercritical H_2 at 23 K and ~ 300 bar), or metal hydrides (H_2 chemisorption, where the T - P range depends on the chosen metal hydride: typically $25 < T < 300$ °C and $1 < P < 10$ bar), many solid porous media have been developed to store H_2 through physisorption interactions.

Among these materials, Metal Organic Frameworks (MOFs), zeolites, carbon-based nano materials have been thoroughly investigated for their hydrogen gravimetric density (i.e. $kg_{H2}/kg_{material}$) reaching up to ~ 9 wt% H_2 at 77 K and 50 bar for these compounds [6–13]. Nevertheless, these materials have several disadvantages such as high production costs [14], complex manufacturing processes [15], low stabilities [16], and high toxicities inherent to their chemical composition and nanostructure [17]. Even more important, hydrogen storage materials based on physisorption process suffer from a dramatic loss of storage capacity as temperature increases above 77 K due to the low enthalpy of H_2 adsorption on these materials, i.e. 5 - 8 kJ/mol [18]. The adsorption capacity of carbon-based nanomaterials typically decreases by one order of magnitude from 77 K to 298 K. For example, H_2 uptake of single-wall carbon nanotubes is ~ 2 wt% H_2 at 77 K and 40 bar, but decreases down to ~ 0.2 wt% H_2 at 298 K and 200 bar [13].

Clay minerals, like smectites, illites or kaolinites, display interesting H_2 adsorption properties and help to overcome some of the above-mentioned limitations. Smectites in particular are promising materials thanks to their abundance in natural environments, their ease of mass production, their large surface area and their high sorption capacities with respect to a plethora of gases, molecules and dissolved ions [19–21]. Smectites are formed by a 2:1 layer made of an octahedral sheet filled by Mg^{2+} cations, in between two tetrahedral sheets (also

* Corresponding author.
E-mail address: lorella.masci@gmail.fr (L. Masci).

https://doi.org/10.1016/j.ijhydene.2023.10.314
Received 1 June 2023; Received in revised form 18 September 2023; Accepted 29 October 2023
Available online 20 January 2024

called TOT layers) filled with Si^{4+} and Al^{3+} cations in the case of saponite (see Fig. 1a). The charge deficit induced by the replacement of Si^{4+} by Al^{3+}, is compensated by interlayer cations, here, Na^{+} or Ca^{+}. The intercalation of H_2 in the interlayer space, may be favored by: i) strong electrostatic interactions inside the interlayer cavities due to the presence of exchangeable cations (this electrostatic field induces a dipolar moment to H_2 - nominally apolar - and thus promotes its physisorption), ii) the geometry of the interlayer space which is homogeneous and does not present bottleneck likely to prevent H_2 diffusion, and iii) the size of the interlayer micropore network that can match a few H_2 diameter (2.89 Å) [22]. Hydrogen may also be adsorbed on the basal and edge sites, and in the porosity in between clay particles. The high specific surface area (SSA) of clay minerals, that can reach ~ 400 m^2/g for some particular clays such as laponite® [22–24], also make them good sorbents for gases like CO_2 and CH_4 [25–29].

Yet, H_2 adsorption capacity of smectites and other clay minerals remains poorly investigated. A maximum gravimetric sorption capacity of ~ 0.2 wt% H_2 was recorded at 77 K and ~ 1 bar H_2 pressure for Al-

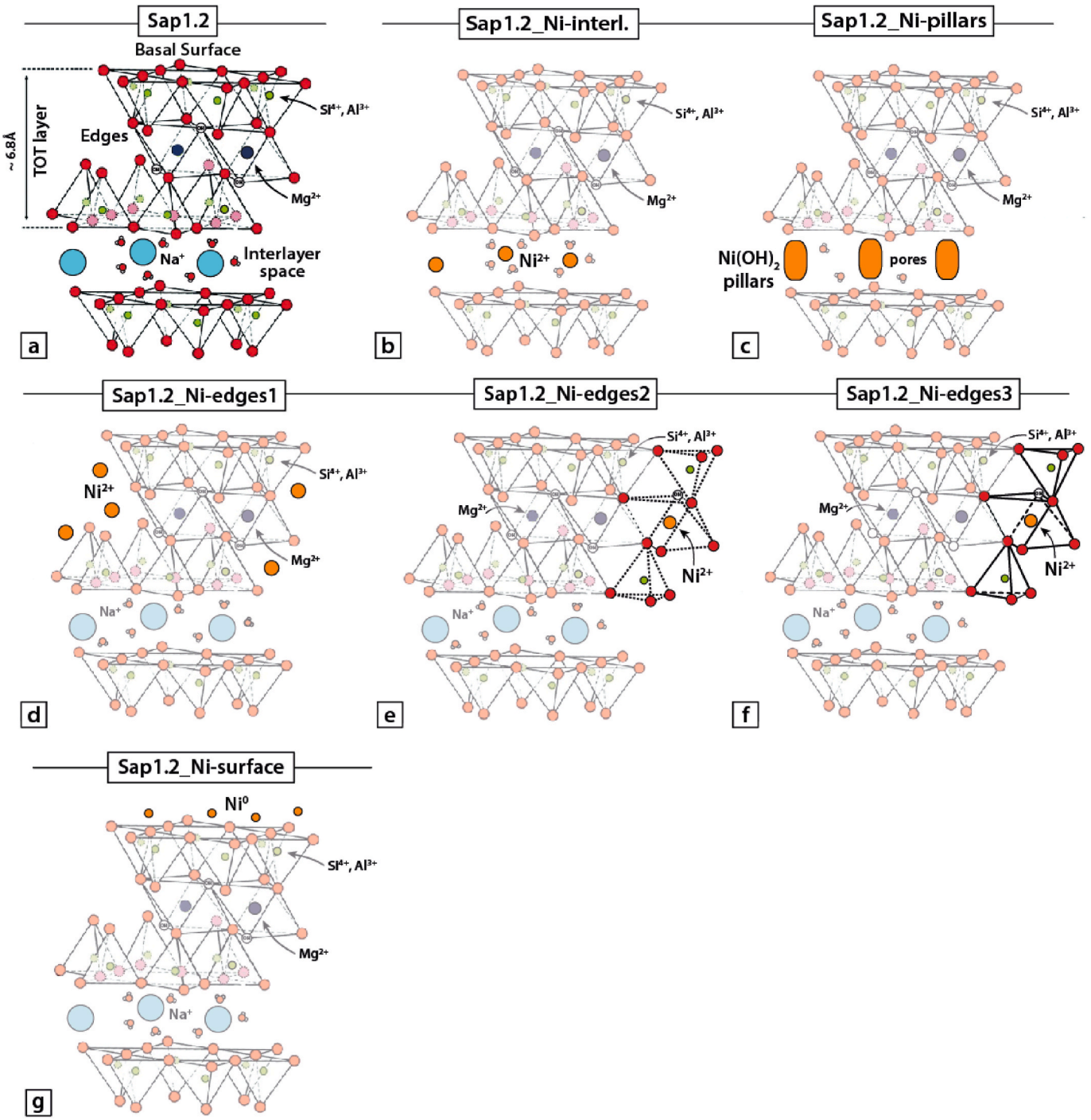

Fig. 1. Crystal-chemical configurations of saponites with Ni addition to the structure (basic structure modified with permission from Paineau et al. [55], after Grim et al. [56]. They are described as followed: a) saponite Na-saturated sample (*Sap1.2*); b) and c) saponites whose interlayer space was modified with Ni^{2+} cations sorption (*Sap1.2_Ni-interl.*), or $Ni(OH)_2$ pillaring (*Sap1.2_Ni-pillars*); d) to f) saponites whose edges were modified with Ni^{2+} sorption (*Sap1.2_Ni-edge1*), partial crystallization (*Sap1.2_Ni-edge2*), or complete crystallization of Ni^{2+} into new octahedral sites (*Sap1.2_Ni-edge3*); g) saponite whose surface was modified by sorption of Ni^0 nanoparticles (*Sap1.2_Ni-surface*).

pillared montmorillonite [30], K-bentonite [31] and sepiolite [32]. Edge and Edge et al. [22,33] studied several varieties of laponite®, which is a registered trademark for a type of smectite, and measured H_2 uptake as a function of temperature and pressure. They reported maximum sorption capacity of ~ 0.1 wt% H_2 at ambient temperature and 140 bar, and up to 0.63 wt% H_2 at 1 bar and 77 K. Recently, Ziemiański & Derkowski [34] investigated H_2 adsorption on montmorillonite and illite at temperatures ranging from 25 °C to 70 °C and pressure up to 145 bar. They concluded that H_2 intercalation within smectite interlayers is strongly dependent on hydration state of the interlayer space, itself controlled by the nature of the exchangeable cation. Under the tested conditions the maximum H_2 uptake never exceeded 0.04 wt%, even if montmorillonite exchanged with tetramethylammonium cation was a noticeable exception displaying an H_2 uptake of 0.1 wt% at 25 °C and 145 bar.

At 77 K, high H_2 sorption values on clays and other porous media are well correlated to the specific surface areas and the micropore volume [32,35,36]. However, it remains unclear whether clay minerals micropores suitable for H_2 adsorption are localized inside the interlayer space, on the edges of the 2:1 layer, on the basal surfaces, or in-between the particles. In addition, the ability of the interlayer space to incorporate gases such as CO_2 strongly depends on both the hydration state, and the nature of the charge-balancing cations [28]. The effect of water content is significant as it might control the space available for gas species adsorption and compete with the sorbent gas. Many studies on clays managed to optimize the interlayer space, by addition of molecular species such as transition metal cations or organic molecules [37–39]. To that extent, pillared clays are the most common type of functionalized clay-based materials as their interlayer space is modified on purpose to create a porous network suitable to enhance the adsorption of a given molecule [30,40–43].

In addition to the effect of porosity, several studies on porous materials highlighted the effectiveness of transition metals such as nickel, in increasing the electrostatic field able to attract and polarize hydrogen atoms on diverse material surfaces [44–46]. Beyond its low cost, compared to classically used H_2-catalysts, like platinum or palladium metals, nickel is a natural component of various types of clays [47,48], and may occupy different crystallographic sites in the clay structure.

As questions remain open on the links between clays porosity and their H_2 adsorption capacity, we focused on the structural properties of a synthetic saponite in order to decipher the crystal-chemical influence on H_2 physisorption. Several saponites were thus synthetized with a carefully controlled addition of Ni^{2+} cations or Ni^0 nano-particles to the structure at different potential H_2 adsorption sites (i.e. interlayer space, edges, basal surface, and octahedral sites) in order to probe the adsorption properties of these sites. In addition, the precursor gel used for saponite synthesis was also tested with respect to its H_2 adsorption properties.

2. Materials and methods

2.1. Sample description

2.1.1. Ni-functionalized saponites

Saponite with the structural composition $Si_{8-X}Al_XMg_6O_{20}(OH)_4Na_X$, a layer charge deficit X = 1.2 (sample named as *Sap1.2*) and a density of d ~ 2.3 g/cm^3 [52] was initially synthetized as a template for Ni functionalization (see protocol at the next section). Two Ni-saponite samples were synthesized by addition of Ni^{2+} into the interlayer space. The first sample, named *Sap1.2_Ni-interl.*, has the structural composition $Si_{6.8}Al_{1.2}Mg_6O_{20}(OH)_4Ni_{0.6}$ with hydrated Ni^{2+} replacing interlayer Na^+ cations. The second configuration, named *Sap1.2_Ni-pillars*, corresponds to the formation of $Ni(OH)_2$ pillars, creating a porous network inside the interlayer space that is supposed to prevent its complete collapse during thermal treatments prior to volumetric analysis [42]. In addition, three different Ni-saponite samples with Ni^{2+} located on the edges were also prepared. According to available protocols [53,54], various duration of sorption experiments led to three samples with different extent of Ni octahedral sheet on particle outer edges: i) with Ni^{2+} cations only adsorbed on the edges of the TOT layer, named *Sap1.2_Ni-edges1*, ii) with partial recrystallization of octahedral and tetrahedral sites from the edges, and Ni^{2+} incorporation into the new octahedral sites, named *Sap_Ni-edges2*, and iii) with complete structural Ni^{2+} recrystallization, named *Sap1.2_Ni-edges3*. An additional configuration was tested by addition of Ni^0 nanoparticles deposited on the surface of *Sap1.2* sheets, and is called *Sap1.2_Ni-surface*. All atomic

Table 1
Description and summary of textural parameters (S_{BET}, $S_{\mu porous}$, $V_{\mu porous}$) and H_2 uptake for all clay materials from this study (*Sap1.2*, Ni-saponites, and *Gel_Sap1.2*), and for standards used in this study and from the literature [22,36,49–51].

with a layer charge of 1.2 e− per O20(OH)4						
Name	S_{BET}	$S_{\mu porous}$	$V_{\mu porous}$	H_2 uptake		Description
				77 K-1 bar	298 K-120 bar	
	m^2/g	m^2/g	cm^3/g	wt% H_2		
CLAYS						
Sap1.2	31	0	0	0.02	0	Ni-free saponite with a charge layer of 1.2
Sap1.2_Ni-interl.	35	0	0	0.02	–	Na^+ exchanged with Ni2+ inside the interlayer space
Sap1.2_Ni-pillars	37	2	0.001	0.01	0	$Ni(OH)_2$ pillars inside the interlayer space
Sap1.2_Ni-edges1	37	3	0.001	0.03	0	Ni^{2+} sorbed on the edges for 2 h
Sap1.2_Ni-edges2	40	6	0.003	0.01	–	Ni^{2+} sorbed on the edges for 12 h
Sap1.2_Ni-edges3	37	2	0.001	0.03	0	Ni^{2+} sorbed on the edges for 22 days
Sap1.2_Ni-surface	9	0	0	0.01	–	Ni^0 nanoparticles on surface
Gel_Sap1.2	145	77	0.029	0.19	0.12	Precursor gel
STANDARDS						
MOF-177	3856	3835	1.547	1.22	0.51	
Furukawa et al., 2007 [17]	4630	n.a.	n.a.	1.25*	n.a.	
Li and Yang, 2007	3100	n.a.	n.a.	1.50	n.a.	
Voskuilen et al., 2012	4126	n.a.	1.67	n.a.	0.55	
Zacharia et al., 2010	3400 - 4100**	n.a.	1.3–1.6	n.a.	0.59	
Activated Carbon	872	523	0.213	1.38	–	
Y-Zeolite	677	630	0.242	0.03	–	
LapRD	347	340	0.239	0.26	0.12	
Edge, 2014	399***			0.24	~ 0.11	

- not measured.
n.a. not available.
* measured at 0.8 bar.
** for densities d = 0.39–0.51.
*** calculated from DFT calculations.
Caption: H_2 modeling applied to H_2 isotherms realized at 77 K.

structures of saponites are shown in Fig. 1, and listed in Table 1. The gel precursor used for the hydrothermal synthesis of Na-saturated saponite, named *Gel_Sap1.2*, was also analysed for its H_2 adsorption properties. The apparent density of the gel was measured volumetrically and was found to be around 1.0 g/cm^3.

All syntheses and analytical measurements were carried out at ISTerre laboratory (Grenoble, France), excepted if clearly mentioned.

2.1.2. Standards

In addition to saponites, several porous materials previously described in the literature have been characterized as N_2 and H_2 adsorption standards to validate our volumetric measurements protocol. A Metal-Organic Framework (*MOF-177*, CAS number 676593-65-0, density d = 0.35 g/cm^3) and an activated carbon (*Activated carbon*, CAS number: 7440-44-0) were purchased from Sigma-Aldrich®. Finally, a zeolite (*Y-zeolite*) was provided by Micromeritics® as an internal standard for N_2 volumetric measurements, and a commercial laponite® (*LapRD*) obtained from Laporte PLC® (ref: 5765) was also used.

2.2. Experimental protocol

Synthesis of saponite (*Sap1.2*) was carried out using hydrothermal method from a sol gel solution according to a well-established protocol [40,57,58], which ensure the purity and particle-size homogeneity of the products. The precursor gel (*Gel_Sap1.2*) was prepared from saturated $Mg(NO_3)_2$ and $Al(NO_3)_3$ solutions, Na_2CO_3, and Tetra Ethyl Ortho Silicate (TEOS) solutions as Mg, Al, Na and Si sources, respectively, in proportions corresponding to the stochiometric formula. The saponite synthesis was achieved at 400 °C and 400 bar of water confining pressure during 4 weeks using an externally heated Morey-type pressure vessel fitted with an internal silver tubing containing 8 g of *Gel_Sap1.2*. After the hydrothermal synthesis, saponite sample was Na-saturated by mixing 1 mol/L aqueous solution of NaCl with saponite for 24 h before separation of the solid fraction by centrifugation (1 cycle of 10 min at 9000 rpm). Excess NaCl was removed by rinsing the solid 4 times with deionized water followed by steps of centrifugation to isolate the solid fraction (4 cycles of 10 min at 12000 rpm).

Part of the resulting crystallized *Sap1.2* was afterwards mixed with a solution of $NiCl_2$ at 0.2 mol/L and matured during 2 × 45 min at ambient temperature, leading to the *Sap1.2_Ni-interl.*.

The *Sap1.2_Ni-pillars* was obtained using an annealing route: an aliquot *of Sap1.2_Ni-interl.* suspension was placed into a 23 mL Parr vessel with NaOH solution at 10^{-5} mol/L at 80 °C for 12 days. As a result, $Ni(OH)_2$ pillars, i.e. isolated "island-like" fragments of a $Ni(OH)_2$ octahedral sheet, were crystallized inside the interlayer space.

Sap1.2_Ni-edges1,2,3 samples were prepared from solutions mixed with Milli-Q® water (conductivity of 18.2 MOhm.cm) and chemicals of ACS reagent grade. The synthesis was conducted in a thermostated glass vessel at 25 °C with constant stirring of the suspension at 250 rpm. An inert atmosphere was maintained by bubbling Ar purified by a solutions setup (H_2SO_4 0.1 M, NaOH 0.1 M and NaCl 0.25 M). 100 mL of *Sap1.2* suspension at 9.1 g/L was added to 39 mL Milli-Q water in which 2.118 g of NaCl salt has been previously dissolved in order to obtain a high ionic strength and to saturate the interlayer space with Na^+. Finally, 1 mL of SiO_2 solution at 0.0725 M was added to compensate the *Sap1.2* dissolution and to allow the epitaxial growth on the edges of the saponite layers [53]. The pH was adjusted and maintained at 7.3 by automated NaOH (0.02 M) addition using a Metrohm® 716 DMS device running with Tiamo™ software. After pH equilibration for 5 h, 5 mL of a solution containing $NiCl_2$ at 23.8 mM and NaCl at 0.25 M was added. The final suspension has a solid-to-liquid ratio of 6.3 g/L, a Ni aqueous concentration of 820 μM, a Si_{aq} concentration of 500 μM and a high ionic strength (NaCl) 0.25 M. Afterwards, three samples of 50 mL of this suspension were collected at 2 h, 22 h and 22 days. Each sample was filtered through a 0.1 μm nitrocellulose filter, washed twice with Milli-Q® water and then freeze-dried.

Saponite decoration with Ni^0 nanoparticles (*Sap1.2_Ni-surface*) was carried out *via* polyol method at LEPMI laboratory (Grenoble, France). Ni^0 nanoparticles were generated from the reduction of dissolved Ni salt in the presence of the *Sap1.2* dispersed in ethylene glycol (EG) that acts as solvent, reducing agent and stabilizer. Addition of monosodium citrate as surfactant allows to better control the size of the particles. In details, 890 mg of $NiCl_2.6H_2O$ and 1.180 g of monosodium citrate were mixed in 100 mL EG in a 250 mL flask. After complete dissolution of the salts, pH was adjusted to 10 by dropwise addition of a 5 wt% solution of KOH in EG. After addition of 175 mg of previously synthesized *Sap1.2*, the mixture was heated under gentle stirring to 160 °C for 20 h. After cooling down to room temperature, the final product was collected by centrifugation (9000 rpm–20 min), rinsed several times with deionized water, and dried at 60 °C for 1 h.

2.3. X-ray diffraction

In order to characterize both the structure and composition of the synthetized Ni-saponites according to their respective protocols, XRD patterns were recorded on powders using a Bruker D8 diffractometer operated in the Bragg-Brentano geometry at 40 kV and 40 mA, and equipped with a SolX Si(Li) solid state detector from Baltic Scientific Instruments®. Intensities were recorded at 0.04° 2θ step intervals from 2 to 20° 2θ range (6 s counting time per step – CuKα_1 + 2 radiation). The diffractometer was also equipped with a MHG Messtechnik® humidity controller coupled to an Anton Paar® CHC + chamber, to perform analyses at various relative humidities (RH = 3 %, 10 % and 80 %).

Powder X-ray diffraction for *Sap1.2* and *Gel_Sap1.2* was also carried out on the MORPHEUS platform of Laboratoire de Physique des Solides (Orsay, France) using a copper rotating anode (RU H3R, Rigaku Corp., Japan) operating at a wavelength λ = 0.1542 nm delivered by Osmic optics. The diffractometer is equipped with a two-dimensional mar345 detector (marXperts GmbH, Germany) with 150 μm pixel size, placed at 150 mm from the sample: glass capillary (1 mm diameter) filled with powder material (saponite or gel). It has been heated inside a furnace at 150 °C for 6 h under primary vacuum conditions and then sealed. The two-dimensional diffraction patterns consist in concentric rings with constant angular intensity. Background signals from air and from the capillary are subtracted based on the measurement of the absorption of the direct beam by the sample. The measured intensity is also corrected from the geometrical factor to be used for a planar detector, the polarisation factor and the X-ray absorption between the sample and a given pixel on the detector.

2.4. N_2 and H_2 adsorption experiments

Unless specifically mentioned, all materials were initially degassed at 150 °C for 6 h under real secondary vacuum at 4 x 10^{-3} mbar. Nitrogen and hydrogen physisorption experiments were carried out at 1 bar and 77 K, using a volumetric gas sorption instrument ASAP 2020 PLUS from Micromeritics Instruments®. From N_2 isotherms, the specific surface area of powdered samples (150 – 500 mg) was estimated using the Brunauer–Emmet–Teller (S_{BET}) equation in the $0.05 \leq P/P0 \leq 0.3$ interval of relative pressure and using a cross-sectional area of 16.2 Å^2 for molecular N_2. For microporous samples, the free space measurements were performed by a BET analysis until P/P0 = 0.4, before outgassing again the samples to prevent He retention previously used for dead volume measurement. Data analyses were performed using ASAP 2020 Plus software from Micromeritics®. The presence of micropores in the sample ($Ø_{pore} < 2$ nm) was assessed using the t-plot method [59].

Hydrogen isotherms were acquired with an equilibration interval of 60 s for routine analysis (~ 5 – 8 h for a complete isotherm acquisition). An ultra-high purity grade of H_2 (99.999 % purity) was used for the adsorption experiments.

High pressure hydrogen experiments were performed at 298 K and 120 bar at the Néel Institute (Grenoble, France) using a PCT Hiden® IMI

system apparatus and data analyses were performed using Isochema® software. Around 200 – 600 mg of powdered samples were inserted inside a steel sample holder (internal volume ~ 200 mm^3), with a small amount of glass wool to prevent powder removal during vacuuming steps. Adsorption and desorption isotherms were performed with an equilibration time of 15 – 30 min for routine analysis. As for low pressure analysis, each sample was heated and outgassed at 150 °C for at least 6 h prior to each measurement.

2.5. Thermogravimetric analyses (DSC-TGA)

TG/DSC curves were recorded on a TGA/DSC3+ Mettler Toledo® instrument. Approximately 50 mg of sample (± 30 mg) were placed in a 150 µL alumina crucible. The experiments were carried out under N_2 atmosphere with a flow rate of 20 mL/min. Sample mass loss and associated thermal effects were recorded from 25 to 900 °C using a constant heating ramp of 5 °C/min. In order to identify the different mass loss steps, the TGA first derivative (rate of mass loss) was used.

2.6. Atomic Force Microscopy (AFM)

Atomic Force Microscopy (AFM) measurements were conducted to measure *Sap1.2* particles topography and particles size. The device used was a MFP-3D microscope with contact mode from Asylum Research® (Santa Barbara, USA). The maximum range of the piezo scanner is 120 µm in the planar direction (x,y) and 15 µm in the vertical direction (z). The microscope is isolated inside a chamber and mounted on top of a vibration isolation control unit from Herzan®. Topography images were acquired in contact mode using triangular silicon nitride (PNP-TR from NanoWorld®) cantilevers with a nominal length of 200 µm, width of 28 µm and a thickness of 500 nm. Before each experiment, the deflection sensitivity was determined and the spring constants were routinely calibrated using the thermal method, resulting in 100 – 200 pN/nm. The obtained data were processed using the AR and WSxM softwares [60].

Prior to AFM measurement, sample of *Sap1.2* was deposited on mica substrate. First, the powder was dispersed in Milli-Q® water (1 mg/mL) and 100 µL of the solution was deposited on the mica plate, dried at room temperature for 1 h and blown with N_2.

2.7. Transmission Electron Microscopy imaging (TEM)

Transmission Electron Microscopy images were acquired using a Jeol® 2010 microscope at the CMTC plateform (Grenoble INP, France) with a LaB_6 filament and operating at 200 kV. The images were collected with a 2048 × 2048 pixels CCD camera (Gatan® Ultrascan 1000 XP).

3. Results

3.1. X-ray diffraction results

XRD measurements on Ni-saponites whose interlayer space was modified with Ni^{2+} exchange (*Sap1.2_Ni-interl.*) or pillaring (*Sap1.2_Ni-pillars*) are displayed in Fig. 2a. At RH = 80 %, Ni intercalation in the structure implies a slight shift of the apparent d_{001}-spacing from 15.12 Å to 14.62 Å and 14.24 Å for cations exchange or pillaring in the interlayer respectively, compared to the initial Na-saturated *Sap1.2*. Without pillaring, decreasing RH from 80 to 10 %, induces noticeable difference between Na-saturated (*Sap1.2*) and Ni^{2+} exchanged saponite (*Sap1.2_Ni-interl.*). One can observe that Ni^{2+} has a higher water affinity than Na^+, as *Sap1.2_Ni-interl.* apparent d_{001}-spacing is still at 14.15 Å at RH = 10 %, while the apparent d_{001}-spacing of *Sap1.2* has already decreased to 12.13 Å, consistently with previous results [61]. Further drying of *Sap1.2_Ni-interl.* down to RH = 3 % leads to a marked decrease of the apparent d_{001}-spacing from 14.15 Å to 12.20 Å. This phenomenon is due

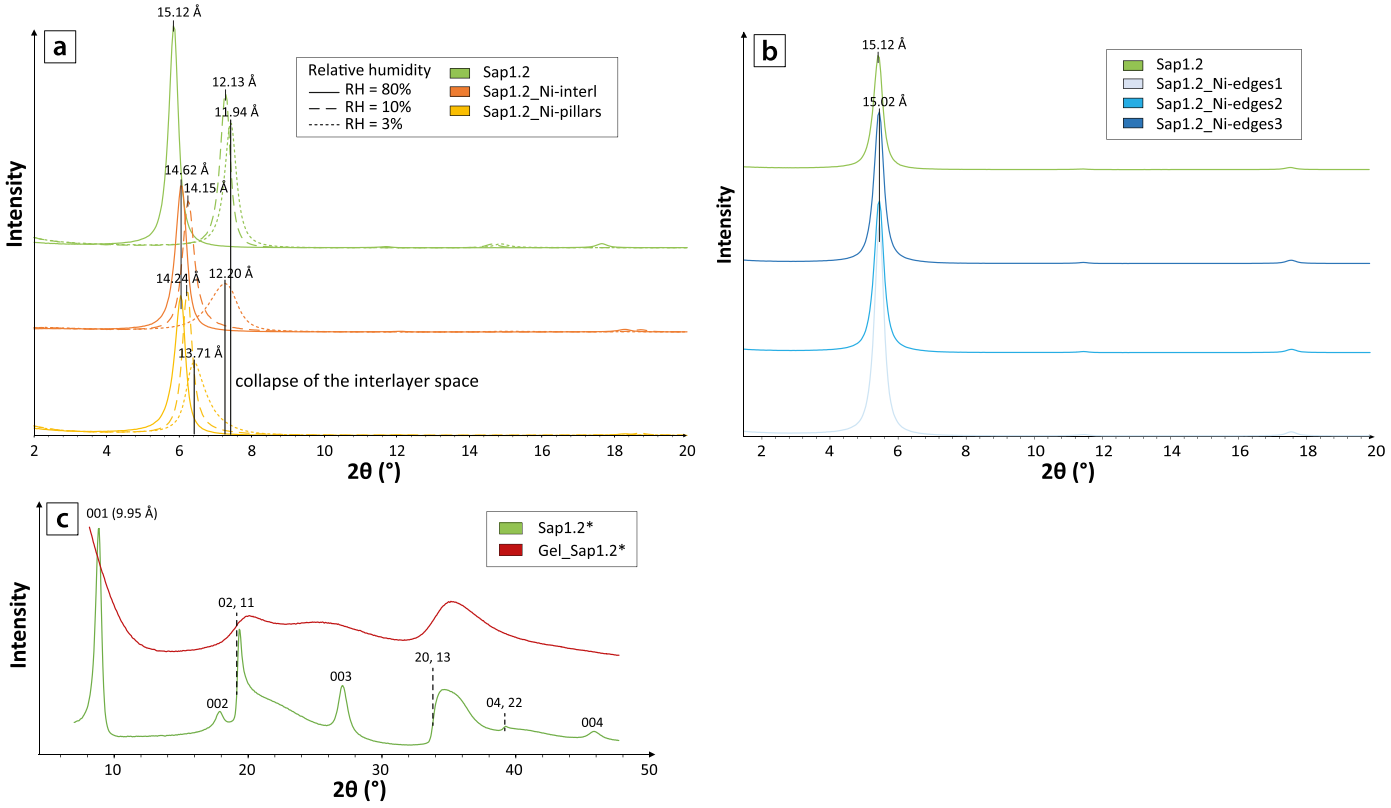

Fig. 2. XRD patterns of Ni-saponites and *Gel_Sap1.2* in comparison with *Sap1.2* (* for capillary measurement): **(a)** Ni-saponites with modified interlayer space (*Sap1.2_Ni-interl.* and *Sap1.2_Ni-pillars*) at different relative humidities RH = 3, 10 and 80 %; **(b)** Ni-saponites whose edges were modified (*Sap1.2_Ni-edges1,2,3*) at RH = 80 %; **(c)** the precursor gel (*Gel_Sap1.2*).

to partial interlayer cation dehydration, and slight differences do exist when Na^+ is exchanged by Ni^{2+} in the interlayer. This is shown by apparent d_{001}-spacing at RH = 3 % of 11.94 Å and 12.20 Å for *Sap1.2* and *Sap1.2_Ni-interl.*, respectively (Fig. 2a). Dehydration phenomenon has only a minor effect on *Sap1.2_Ni-pillars*, whose apparent d_{001}-spacing is 14.24 Å at RH = 80 % and 13.71 Å at RH = 3 %, confirming the presence of $Ni(OH)_2$ pillars in the interlayer space. Indeed the presence of these pillars prevents the collapse of the interlayer as previously reported [62].

Saponites whose edges were modified by nickel addition (i.e. *Sap1.2_Ni-edges1,2,3)* evidence almost no apparent d_{001}-spacing shift compared to *Sap1.2* at RH = 80 %, with d = 15.02 Å for the three samples and d = 15.12 Å for *Sap1.2* (Fig. 2b). This observation validates our experimental protocol, as it confirms incorporation (adsorbed or incorporated) of Ni^{2+} cations on the edges and not inside the interlayer space. In Fig. 2a and b, only the 00*l* reflections are observed due to the geometry of the experiment and the use of oriented preparations.

The powder X-ray diffractogram of *Sap1.2* is shown in Fig. 2c. One observes the 00*l* reflections characteristic of the stacking of the TOT sheets. In addition, *hk* bands with typical sawtooth profiles are observed rather than *hkl* reflections owing to turbostratism (systemic occurrence of stacking disorder in between successive layers). The in-plane coherence lengths are given by the slope of the rising edge of the bands [63]. It is resolution limited here, which only allows us to conclude that they are larger than a few tens of nanometer. The 02,11 and 20,13 bands are still visible for *Gel_Sap1.2*, with a much smoother rising edge however, indicative of very small fragments of octahedral/tetrahedral sheets constitutive of TOT layers, and representative of a nano-crystallized component. An additional broad and symmetric hump centered at $2\theta \approx 25^\circ$ is also observed, which may correspond to an amorphous gel component. No 00*l* peak is observed, due to the intense signal at small angles reflecting the porosity of the assembly of these small solid particles (Fig. 2c).

3.2. AFM and TEM imaging

Fig. 3a–d shows topography and deflection AFM images of a continuous film of *Sap1.2* deposited on a mica plate. Topography images provide very precise information on the height variations of the sample surface and deflection images provide a better observation of the height changes. Images acquired at a spatial scale from 3 to 0.6 µm and resolution around from 10 to 2.5 nm/px revealed the stacking of *Sap1.2* layers forming round to more hexagonal shapes from 150 nm to 600 nm in diameter for the biggest grains (Fig. 3c and d). Fig. 3e shows a statistical analysis of the topography data using a height histogram. The stacking of the saponite layers with an average height of 21.5 nm is in good agreement with the stacking length deduced from powder XRD measurements. Furthermore, this histogram shows small variations of height distribution of about 1.35 nm (see inset of Fig. 3e) which is compatible with the d values deduced from XRD for smectite monolayers. This result agrees well with the direct measurement of the height profile performed on the single TOT in Fig. 3c (highlighted with a green

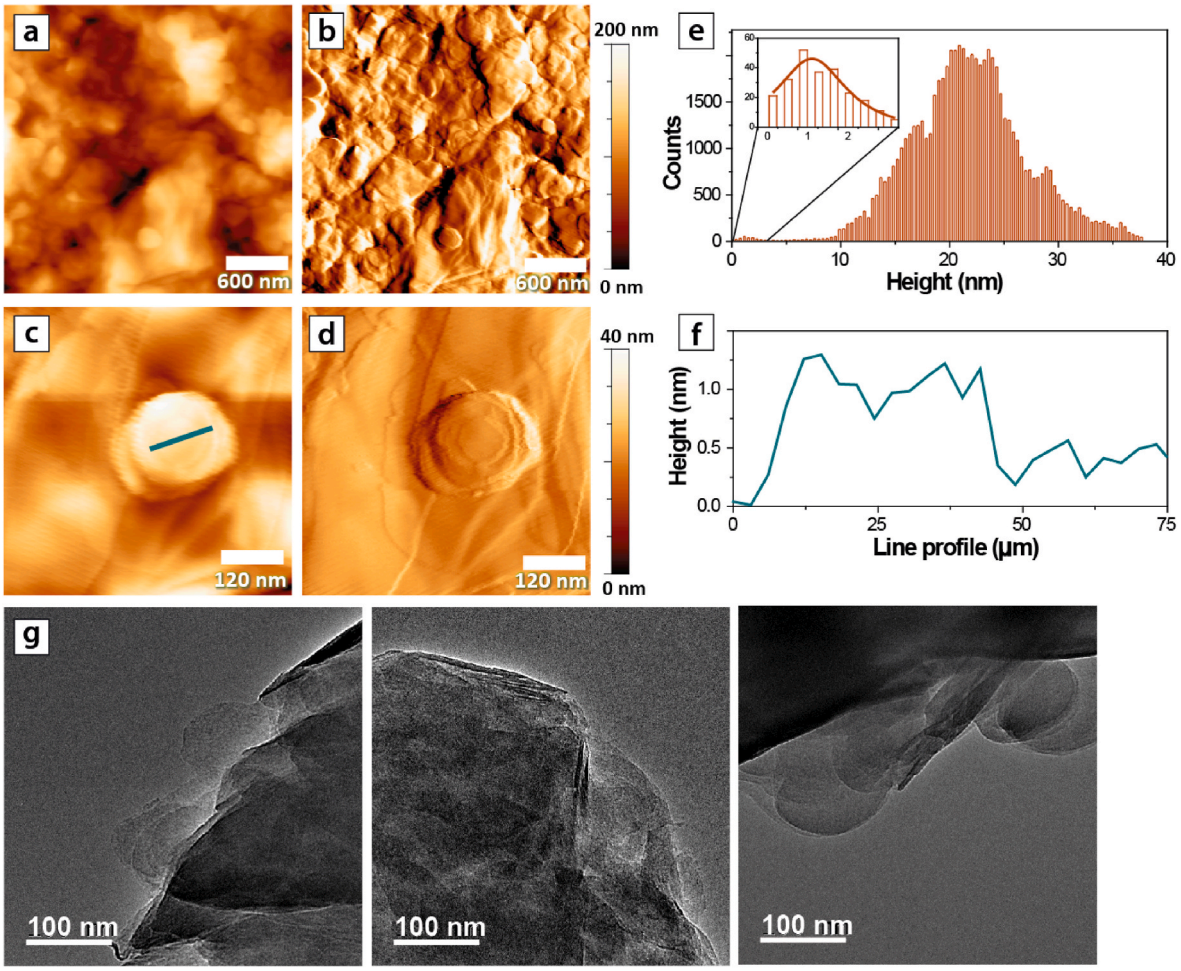

Fig. 3. Topographical AFM images of *Sap1.2*: **(a,c)** height images and **(b,d)** deflection images of the saponite layers deposited on mica substrate. **(e)** Height histogram of Fig. 3c showing the size of the agglomerations and the inset showing the distribution for the smallest height. **(f)** Height profile corresponding to the horizontal lines in Fig. 3c which corresponds to the topography of a single (mainly rounded) saponite layer. **(g)** TEM images of *Sap1.2*.

line) and reaching height variation between 1.1 and 1.2 nm, as displayed by the height profile of Fig. 3f.

TEM images show an almost hexagonal grain shape of the clay sheets for *Sap1.2*, with grain sizes reaching 400 nm in diameter for largest grains on measured areas (Fig. 3g). More circular-shaped grains with average grain sizes around 100 nm can also be observed (Fig. 3g, right). These observations are well consistent with grain shapes and sizes described previously with the AFM technique.

3.3. TGA results

All samples (*LapRD*, *Sap1.2*, *Sap1.2_Ni-interl.*, *Sap1.2_Ni-pillars, and Sap1.2_Ni-edges1,2,3*) show a major weight loss of 6 – 14 % from ~ 100 °C up to ~ 250 °C (Fig. 4) corresponding to the removal of interlayer water. The overall amount of water release depends on the initial hydration state, which is imposed by the RH of the room atmosphere prior to the measurement. The *Sap1.2* on the one hand, and both the *Sap1.2_Ni-interl.* and *Sap1.2_Ni-pillars* on the other hand display different water loss at 150 °C: ~ 9 and 14 wt%, respectively. More water is attracted and retained by Ni^{2+} and $Ni(OH)_2$ pillars than by Na^+ whose hydration energy is lower. However, as RH was not controlled, the overall amount of water release mainly depends on the initially lower hydration state of *Sap1.2* compared to the Ni-saponites. In addition, *Sap1.2_Ni-interl.* and *Sap1.2_Ni-pillars* display a second small weight loss of ~ 2 % around 200 °C, and a third loss < 1 % around ~ 400 °C. Such a phenomenon is only observed for samples with interlayer Ni. The small weight loss at 200 °C may correspond to the dehydration of remaining water linked to Ni^{2+} or $Ni(OH)_2$ pillars. Indeed in the case of *Sap1.2_Ni-interl.*, Ni^{2+} cations have the ability to partly retain H_2O molecules from its hydration sphere along dehydration [64,65]. The weight loss observed at 400 °C is well explained by the thermal decomposition of the $Ni(OH)_2$ pillars [66]. However, in the case of *Sap1.2_Ni-interl.*, it is possible that water produced during the two firsts dehydration steps at 150 °C and 200 °C, further reacts with Ni^{2+} in the interlayers to form $Ni(OH)_2$ pillars during the TGA measurement. The dehydration of these latter pillars explaining the small weight loss observed at 400 °C for *Sap1.2_Ni-interl.*. Finally, another major weight loss is also recorded for all samples at temperature above 700 °C corresponding to the dehydroxylation process, i.e. the loss of OH groups from the structure, which is well-described for trioctahedral smectites at these temperatures [67–69]. It can also be reported that *LapRD*, shows a slightly lower dehydroxylation temperature starting at ~ 700 °C. This shift likely results from the smaller particle size of *LapRD* compared to saponite, thus improving the diffusion of water molecules [70].

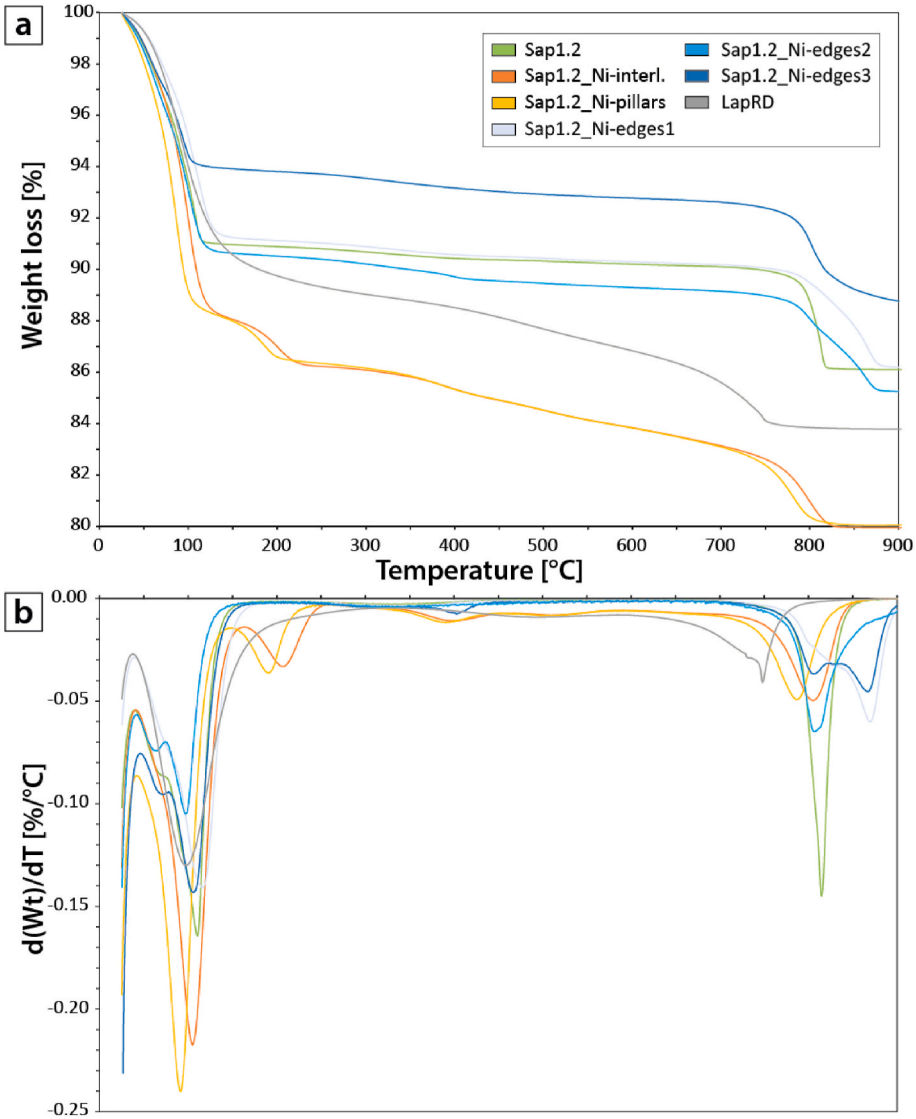

Fig. 4. TGA and DTG profiles of Ni-saponites, *Sap1.2* and *LapRD*. Analysis were carried out from 25 °C to 900 °C at a ramp heating of 5 °C/min.

3.4. N_2 isotherms and textural characterization

Calculations of specific surface area give i) a S_{BET} = 31 m^2/g for *Sap1.2*, ii) a range of S_{BET} from 35 to 40 m^2/g for most of Ni-saponites, and iii) a S_{BET} of 9 m^2/g for *Sap1.2_Ni-surface* (Table 1). The N_2 isotherms of well-crystallized Ni-saponites are difficult to classify according to the IUPAC (International Union of Pure and Applied Chemistry) terminology (Fig. 5). On the one hand, their global shape present isotherms of type II, characteristic of non-porous materials [71]. The t-plot calculations also indicate the absence of microporosity (e.g. surface and volume of micropores close to zero). On the other hand, the presence of hysteresis loops typical for isotherms of type IV indicate capillary condensation effects occurring inside the pore space of the samples (Fig. 5a–d). Here, all saponites show hysteresis loops of H3/H4 types from the IUPAC classification, typical of platy-shaped particles (H3) such as clay minerals [72]. The BJH, HK and DFT calculations were not applied on saponite, as the lack of conventional porosity from N_2 isotherms, i.e. micro- or mesoporosity from the IUPAC classification, could lead to erroneous pore size distributions.

N_2 isotherm of *Gel_Sap1.2* differs significantly from other well-crystallized saponite samples as it displays a clear shape of type I at low relative pressures, which indicates the presence of microporosity (i.e. pore size < 2 nm). It can be related to the intensity increase at small angle in XRD experiments. This is supported by t-plot calculations that give the following surface and a volume of microporosity: $S_{\mu pores}$ = 77 m^2/g and $V_{\mu pores}$ = 0.029 cm^3/g. The specific surface area calculation gives a S_{BET} of 145 m^2/g, which is up to 4 times higher than for its crystallized counterpart *Sap1.2*. Hysteresis loops also reveal capillary condensation in *Gel_Sap1.2* porous structure.

3.5. H_2 adsorption isotherms

3.5.1. Assessment of H_2 adsorption procedures

Both low and high H_2 pressure isotherms were carried out on *MOF-177, Activated carbon, Y-zeolite* and *LapRD*, to compare H_2 uptakes with data from literature (Fig. 6; Table 1). At 77 K–1 bar, the *Activated carbon* and *MOF-177* display the highest H_2 uptakes with 1.38 and 1.22 wt% H_2, respectively (Fig. 6a). For *MOF-177*, our H_2 isotherm indicates a slightly lower uptake than that reported previously [49,50] at 77 K and around 0.8 bar (1.50 wt%). At high pressure (> 100 bar) and 298 K, the comparison of H_2 isotherms from this study and from the literature [22,36,51] for both *MOF-177* and *LapRD*, show a very good agreement with H_2 uptake of 0.12 and 0.50 wt% H_2 at 120 bar and 298 K for *LapRD* and *MOF-177*, respectively (Fig. 6b).

Specific surface areas were derived from N_2 isotherms and BET calculations. Our measurements give a S_{BET} of 3856 m^2/g for *MOF-177*, consistent with values from literature that range from 3100 to 4630 m^2/g (see Table 1 and references therein). *Activated carbon* and *Y-zeolite* show S_{BET} of 872 and 677 m^2/g, respectively, in good agreement with available data [13,73]. *LapRD* has a S_{BET} of 347 m^2/g, which is consistent with the previous value from Edge [22] of 399 m^2/g calculated from DFT calculations on the same laponite (Table 1).

Slight bulk material density differences in-between these different studies may lead to minor changes of the microporous networks. By way of consequence, S_{BET} and H_2 uptake may slightly vary from one preparation to other, as illustrated by the mechanically-densified *MOF-177* from Zacharia et al. [51]. In addition, as outgassing conditions are not always identical from one study to the other, direct comparison with data from literature may not be straightforward. Whatever it is, the present benchmark exercise indicates a satisfactory agreement between our data and those available in state-of-the-art studies under similar operating conditions, thus validating the procedures used in the present

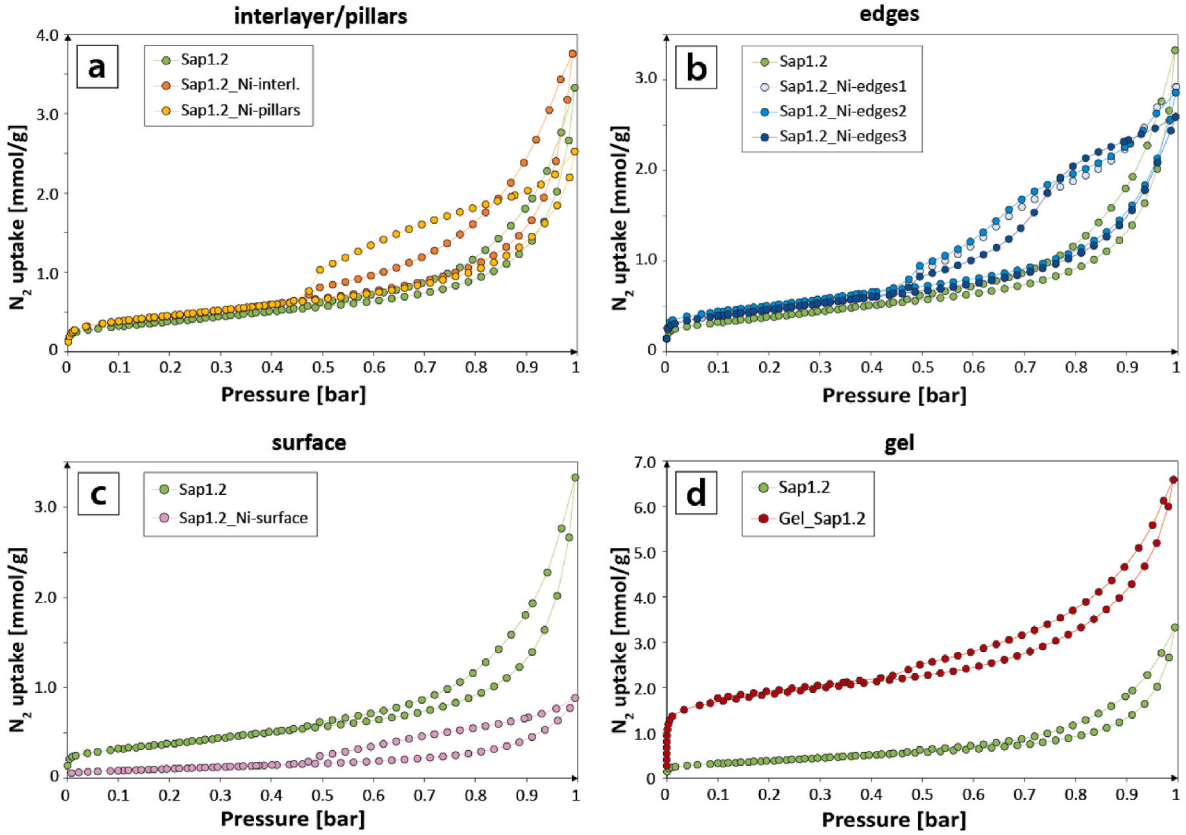

Fig. 5. N_2 isotherms carried out at 1 bar and 77 K of *Sap1.2* compared to: **(a)** *Sap1.2_Ni-interl.* and *Sap1.2_Ni-pillars*; **(b)** *Sap1.2_Ni-edges1,2,3*; **(c)** *Sap1.2_Ni_surface*; and **(d)** *Gel_Sap1.2*. All samples were outgassed at 150 °C prior to analysis.

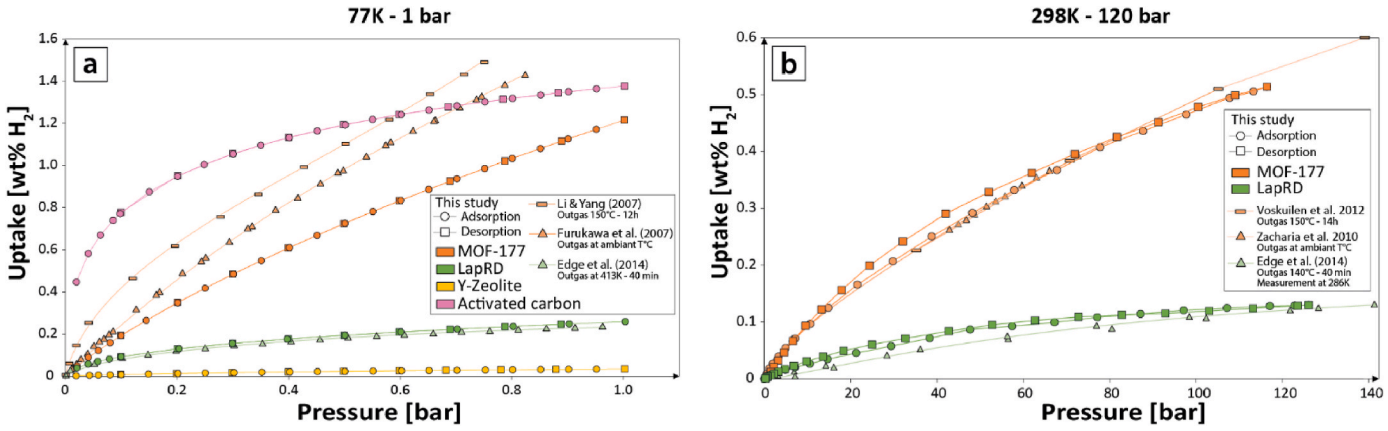

Fig. 6. H_2 isotherms of standards *MOF-177*, *LapRD*, *Y-zeolite* and *Activated carbon* from this study and from the literature [22,36,49–51] carried out at: **(a)** 77 K and 1 bar; and **(b)** at 298 K and 120 bar. LapRD from Edge [22] is a Na-LaponiteRD similar to *LapRD* from this study.

work.

3.5.2. H_2 isotherms of saponite and gel samples at 77 K - 1 bar

H_2 isotherms of saponites at 77 K – 1 bar show H_2 uptakes ranging from 0.01 to 0.03 wt% H_2 for *Sap1.2_Ni-pillars* and for *Sap1.2_Ni-edges1*, respectively. These slight uptake differences being within the uncertainty (around ± 0.01 wt% H_2 at 1 bar, calculated from *LapRD* reproducibility measurements), no significant increase of H_2 uptake capacity could be identified for Ni-saponites compared to *Sap1.2* whose H_2 uptake stands at 0.02 wt% (Fig. 7a–c).

The precursor gel *Gel_Sap1.2* is a significant exception with a maximum uptake of 0.19 wt% H_2 at 1 bar H_2 pressure, which is by one order of magnitude higher than the capacity of *Sap1.2* under the same conditions (Fig. 7d).

3.5.3. H_2 isotherms of saponite and gel samples at 298 K – 120 bar

H_2 isotherms acquisition at high pressure on these materials can be very challenging as the following pitfalls must be overcome: (1) gas leakage due to the high diffusivity of H_2, (2) a low signal to noise ratio due to the low H_2 uptake capacity combined with low S_{BET} of most saponite samples, and (3) poorly-resolved volumetric due to the small mass of saponite (~ 250 mg) that can be loaded in the ~ 200 mm^3 sample holder. Having in mind all these limitations, one can conclude from Fig. 8a that H_2 uptake on saponites, with and without Ni^{2+} in the structure, is very low, remaining < 0.05 wt% for all saponite samples investigated.

Contrastingly, the precursor gel *Gel_Sap1.2* shows a maximum H_2 uptake of 0.12 wt% H_2 at 120 bar and 298 K, and a very good reproducibility between the two replicate measurements performed of the same sample (Fig. 8b).

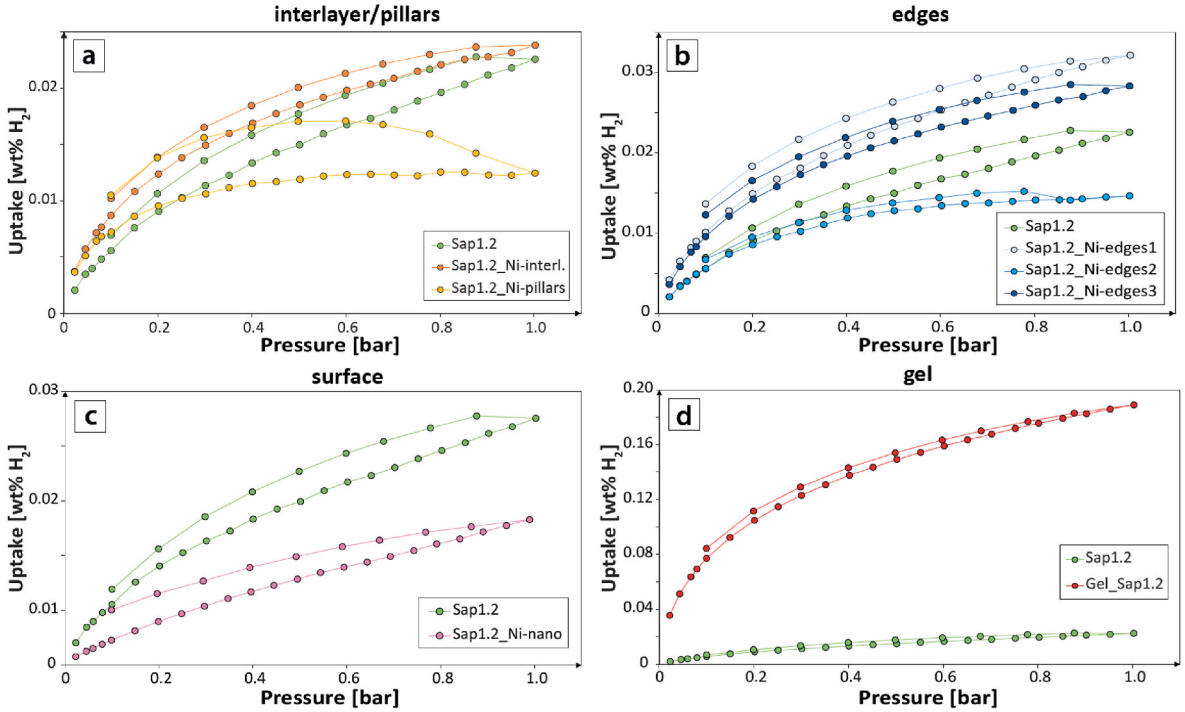

Fig. 7. H_2 isotherms carried out at 1 bar and 77 K of *Sap1.2* compared to: **(a)** *Sap1.2_Ni-interl.* and *Sap1.2_Ni-pillars*; **(b)** *Sap1.2_Ni-edges1,2,3*; **(c)** *Sap1.2_Ni_surface*; and **(d)** *Gel_Sap1.2*.

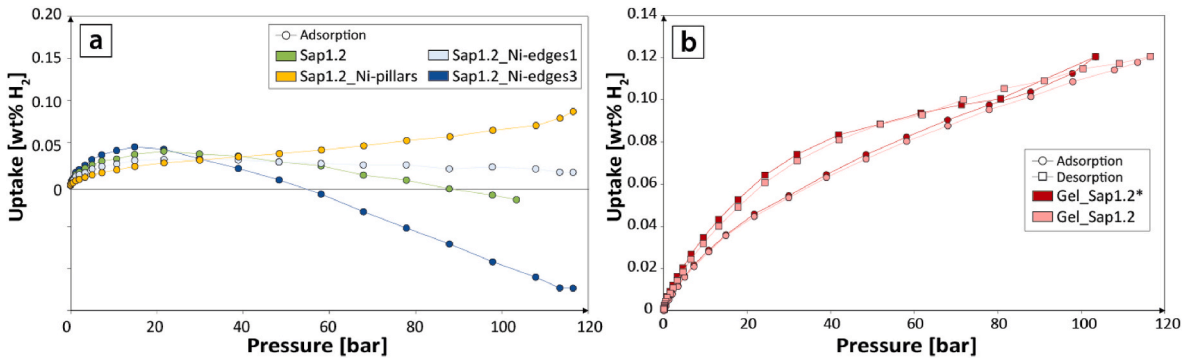

Fig. 8. H_2 isotherms carried out at 120 bar and 298 K on: **(a)** *Sap1.2, Sap1.2_Ni-pillars, Sap1.2_Ni-edges1,3*; and **(d)** *Gel_Sap1.2* and *Gel_Sap1.2** (replicate), whose isotherm was measured on the same apparatus.

4. Discussion

4.1. Effect of porosity and Ni^{2+} intercalation on H_2 adsorption on saponite and nano-crystalized precursor at 1 bar – 77 K

At 1 bar and 77 K, all saponites show H_2 uptakes from 0.01 to 0.03 wt % H_2 and no clear tendency is highlighted in between Ni-saponites that could be assigned to a specific Ni configuration in the structure. The *Gel_sap1.2* shows a higher H_2 sorption capacity with a H_2 uptake of 0.19 wt% H_2 at 1 bar - 77 K. Only few data from literature are available on smectite H_2 sorption capacities [30,74,75]. Gil et al. [30] recorded ~ 0.2 wt% H_2 at 1 bar and 77 K on an Al-pillared montmorillonite. These high uptakes are correlated with the presence of microporosity whose volume (as determined by N_2 adsorption) reaches up to 0.080 cm^3/g, which is well above values ~ 0.001–0.003 cm^3/g determined for Ni-saponites in the present study (Table 1). The apparent hysteresis on saponite N_2 isotherms (Fig. 5) is likely produced by inter-particles pore space, corresponding to a more complex porous network in comparison to conventional mesoporosity [76,77]. This is confirmed by the absence of a sorption plateau at P/P0 = 1. Here, the desorption curves of *Sap1.2_Ni-pillars* and *Sap1.2_Ni-edges1,2,3* display hysteresis loops larger than for *Sap1.2* and *Sap1.2_Ni-interl.*, while having similar adsorption branches (Fig. 5). As these samples cannot be considered as microporous, it is difficult to interpret these differences in term of pore geometries as classically commonly assumed [78]. However it is likely that Ni^{2+} and $Ni(OH)_2$ clusters/pillars affect *Sap1.2* structure in a sufficient manner to impact capillary condensation during desorption by two main aspects: (1) the variation of hydration energy of smectite interlayer cation (*Sap1.2_Ni-interl.*); and (2) the creation of "holes" in between pillars that may remain hydrated even at very low RH conditions (*Sap1.2_Ni-pillars*) as attested by the weight loss attributed to interlayer water removal above 150 °C (Fig. 4). In fact, intercalation of Ni^{2+} in the saponite structure mainly influences water retention as revealed by XRD and TGA data. Such effect is particularly visible for both the *Sap1.2_Ni-interl.* and *Sap1.2_Ni-pillars* (Figs. 2 and 4). However, there is no increase of H_2 adsorption through the creation of Ni^{2+}-bearing crystallographic sites compared to the Na-saturated *Sap1.2*.

Concerning the *Sap1.2_Ni-surface* sample, the lower SSA may be explained according to Sarac Oztuna et al. [79]. The SSAs of functionalized porous subtract are slightly lower than that of bare subtract because of pore clogging by nanoparticles. However, these authors have observed that the SSA gradually increased when Ni nanoparticles loading increases from 1.5 wt% to 20 wt%. Therefore, Ni amount may be optimized in order to minimize the SSA reduction while providing the catalytic performances of metal loading.

The *Gel_sap1.2* is an exception as its micropores volume (0.029 cm^3/g, as determined by N_2 adsorption) is much higher than the one of the well-crystallized saponites, but remains relatively small for such a high H_2 uptake. This observation questions either the importance of the textural control on H_2 adsorption or the relevance of N_2 adsorption results to characterize the micropore volume available for H_2, as discussed below.

4.2. Effect of outgassing condition

Outgassing conditions, i.e. temperature and duration of the outgas prior to volumetric measurements, have a strong impact on H_2 adsorption, as highlighted by Edge [22] study on laponite who tested different degassing temperatures (from ambient temperature, and up to 160 °C under secondary vacuum condition) and observed very different H_2 uptakes (from 0.08 to 0.24 wt% H_2). Ziemiański & Derkowski [34] also reveal that H_2 uptake on montmorillonite significantly decreases with increasing outgassing temperature from 40 to 210 °C. Here, sample outgassing at 70 °C, 150 °C, and 300 °C were carried out on *Sap1.2_Ni-pillars* in order to evaluate the effect of outgassing temperature on H_2 adsorption (Fig. 9). In particular, the thermal treatment during outgassing impacts the hydration state inside the interlayer space. Here, a temperature outgas of 70 °C, instead of a routine 150 °C treatment, results in a significant sorption capacity increase from 0.05 wt% to 0.12 wt % H_2 at 77 K and 1 bar. Adsorption isotherms recorded after outgassing the sample at 150 °C or 300 °C are nearly identical. As previously observed from TGA results on this sample, dehydration is initiated at low RH and nearly fully completed at ~ 150 °C, and dehydroxylation of $Ni(OH)_2$ pillars occurs at ~ 400 °C. Then it is likely than sample outgassing at 150 °C or 300 °C lead to a partial or complete dehydration of *Sap1.2_Ni-pillars* interlayer space, leading to its collapse despite the presence of pillars in between. Then such a collapse may prevent H_2 and N_2 to access these sorption sites. On the contrary, outgassing at 70 °C may allow the preservation of the pillars structure. In this case, the d_{001}-spacing remains at about 14 Å. This value compares with 9.35 Å in

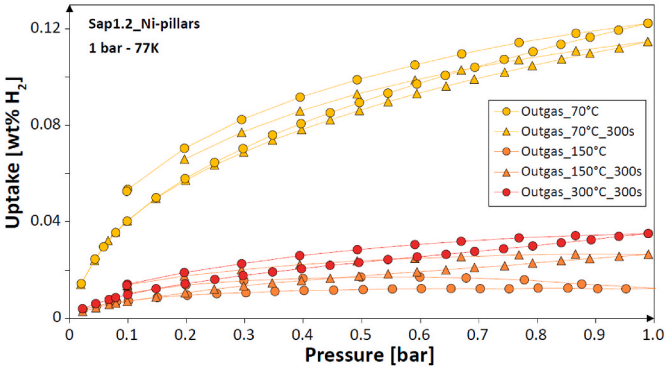

Fig. 9. H_2 isotherms at 1 bar and 77K of *Sap1.2_Ni-pillars* at various outgassing and analysis conditions. Outgas temperatures of 70 °C, 150 °C, and 300 °C were tested, and equilibration time was increased to 300 s instead of 60 s.

the uncharged anhydrous analogue, talc. Because of the $Ni(OH)_2$ pillars, the interlayer height of *Sap1.2_Ni-pillars* is therefore d = (14 - 9.35) Å = 4.65 Å. This value is slightly higher than the kinetic diameter of H_2 (2.89 Å) and may be close to the optimum for H_2 to access the interlayer sorption sites [80]. These measurements nicely demonstrate the importance of the interlayer height for H_2 adsorption and the benefit of $Ni(OH)_2$ pillaring. We note that water hydration also allows to tune the interlayer height and may thus promote H_2 adsorption [28,34]. However, the outgassing step (heat and vacuum), that is a prerequisite before carrying out adsorption isotherms, may compromise a proper control of the hydration state of the samples as demonstrated by all our measurements performed after outgassing at 150 °C (Fig. 7).

In addition, a higher equilibration time (i.e. t = 300 s at each pressure increment instead of routine analysis t = 60 s, resulting in > 30 h of acquisition time for a complete isotherm) was also tested to evaluate H_2 adsorption kinetic. Indeed, H_2 diffusion to the adsorption site may also have to be accounted for the adsorption properties of the material. However, no positive effect related to the equilibration time was clearly recorded here on H_2 uptake.

4.3. Effect of SSA influence on hydrogen adsorption capacity in porous materials

Several studies have already revealed the linear relationship between H_2 adsorption and the specific surface area at 1 bar and 77 K on different types of porous materials [35,81,82]. Such a trend is also observed here (Fig. 10, colourful symbols), up to almost 500 m^2/g for the upper SSA range corresponding to laponite.

It is quite clear that samples having a high SSA, also display a high microporosity. In the case of both *LapRD* or *Gel_Sap1.2* the $S_{\mu pore}$ (340 m^2/g and 77 m^2/g) stand for ~ 98 % and ~ 50 % of S_{BET} (347 m^2/g and 145 m^2/g), respectively (Table 1). Such a conclusion has also been reached previously [36] for MOFs and activated carbons. Therefore, it is likely that micropores are responsible for much of the H_2 adsorption capacity. This observation makes sense when considering that a good match in-between micropores and H_2 kinetic diameter (2.89 Å) is a prerequisite for enhanced H_2 adsorption.

We also point out that N_2 BET measurements do not allow probing the interlayer space. Thus, it is coherent that clay samples whose interlayer space has collapsed because of outgassing at 150 °C are all plotted along this linear correlation in between H_2 adsorption and the specific surface. It also explains why *Sap1.2_Ni-pillars* outgassed at 70 °C, whose interlayer is still accessible to H_2, plots well above this line.

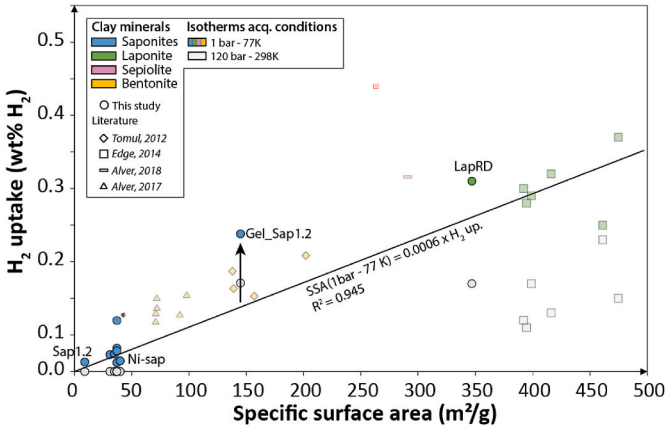

Fig. 10. H_2 uptakes of clay minerals from this study and the literature at 1 bar - 77 K and 120 bar – 298 K. The linear trend correlating SSA and H_2 uptake was calculated at 1 bar - 77 K for saponite and laponite. *: *Sap1.2_Ni-pillars* with temperature outgas of 70 °C.

4.4. Performance of saponite and related gel at 120 bar–298 K

All saponites show H_2 uptakes < 0.05 wt% at 120 bar and 298 K, and the *Gel_sap1.2* shows a higher H_2 sorption capacity of 0.12 wt% H_2. At ambient temperature and above, Mondelli et al. [74] and Bardelli et al. [75] recorded H_2 sorption capacities of ~ 0.20 and 0.25 wt% H_2 at 90 °C and 80 bar H_2 pressure on Na-montmorillonite and purified clay fraction (mainly illite-smectite) of a Callovo-Oxfordian claystone, respectively. However, these values are intriguing for two reasons. First, they are very high regarding both the elevated temperature condition and the low specific surface area of these materials (< 40 m^2/g). Second, they slightly increase with temperature from 28 to 90 °C [75], which is not thermodynamically consistent. Recently, Ziemiański & Derkowski [34] indicated that H_2 uptake on montmorillonite having 60 < S_{BET} < 130 m^2/g does not exceed 0.02 wt% at 298 K and 145 bar. They also confirmed that this H_2 uptake logically decreases significantly with temperature increase.

The linear relationship in between S_{BET} (as measured by N_2 adsorption) and H_2 uptake does not seem to be valid at high pressure and ambient temperature (Fig. 10, grey symbols). H_2 sorption capacities drastically decrease as temperature increases, and that pressure increase does not compensate for this decrease. In the case of saponite, H_2 uptake is below 0.05 wt% H_2 at 298 K and 100 bar. Clay-related materials with higher S_{BET}, like *Gel_Sap1.2* and laponites (*LapRD*; [22]), do adsorb modest amount of H_2 under such conditions (> 0.2 wt%), but SSA in itself is not sufficient to predict their H_2 adsorption capacity. For example, the *Gel_Sap1.2* shows similar H_2 uptake at 120 bar and 298 K than laponites despite contrasting SSA values (SSA = 145 and 392 – 475 m^2/g, respectively). Thus, the SSA and micropore volume determined by N_2 adsorption does not seem to be relevant to characterize the properties of the materials with respect to H_2 adsorption, at least at high pressure and ambient temperature. Ziemiański & Derkowski [34] clearly reveal that micropore volume determined by CO_2, a molecule that display a kinetic diameter closer to H_2 (2.89 and 3.3 Å for H_2 and CO_2 respectively), is much more appropriate.

4.5. Gels of clays: new perspectives for H_2 sorption ?

The emphasis for much research on H_2 storage has been placed in the limiting requirements for mobile applications, hitherto excluding clays because of their intrinsic weight. But large-scale storages do not bear the same constraints. In this context, clay minerals have several very attractive properties such as large surface area, low cost, and environmental safety. Representing volumetric density (i.e. kgH_2/m^3) instead of gravimetric density (i.e. wt% H_2) is particularly relevant when comparing different materials, as their mass densities may be very different. Fig. 11 compares H_2 storage capacities at 298 K, a temperature of interest for large scale storage, for both *Gel_Sap1.2* and the well-studied *MOF-177*, at two different pressure: 30 and 120 bar. First, by strictly comparing their volumetric density, i.e. their mass capacity for storing H_2 in a given volume (here 1 m^3), *Gel_Sap1.2* shows a comparable performance with *MOF-177*. In particular, at 30 bar and 298 K both materials have nearly identical H_2 volumetric densities of 0.5 kgH_2/m^3. Ambient temperature associated with a few tens of bars being ideal conditions for an industrial application, like a stationary underground H_2 storage, it is thus interesting to notice the high potential of *Gel_Sap1.2*.

Even if MOFs, as well as *Gel_Sap1.2,* do not display sufficient H_2 uptake to make them useful for H_2 storage at ambient temperature, one may notice that a low cost and easy-to-produce material like gel performs as well as very expensive MOFs. Thus, this gel of clay material is a new and promising porous material. Its sorption capacities may be enhanced by compaction (increase the volumetric density) and by acid treatment, as classically used for enhancing specific surface area [32].

Up to now, all the research effort on H_2 physisorption has focused on crystallized nano-materials (e.g. MOFs, zeolites, carbon nano-fibers)

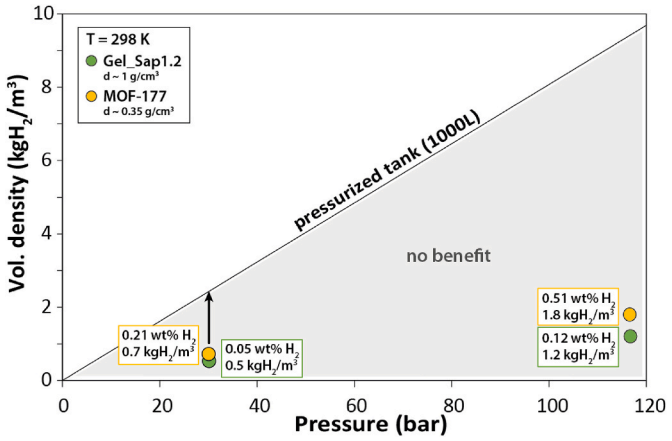

Fig. 11. Hydrogen volumetric densities of *Gel_Sap1.2* at 30 bar and 120 bar compared to *MOF-177* at ambient temperature. The black arrow indicates the density objective to reach to have an economic interest in storing H_2 physisorbed inside clays instead of gaseous storing in pressurized tank.

whose pore size is dimensioned to approach the kinetic diameter of the H_2 molecule. The alumino-silicate gel displays sorption capacities that are 2 – 5 times higher than their crystalline equivalent, even at ambient temperature. By definition, the so call *Gel_Sap1.2* is supposed to be amorphous, but XRD patterns (Fig. 2c) attest for the presence of small or poorly crystalline phases. In addition, it displays high specific surface area (~150 m^2/g) and high micropore volumes ($V_{\mu pores} = 0.029\ cm^3/g$). This "gel" is therefore the antithesis of all crystallized substrates studied so far. A specific point to further investigate to better understand the global structure of this material and more specifically the localization of micropores. Its ambient sorption properties are still too low to justify a stationary storage application, but an improvement in its capacity by a factor of 2 would already allow a significant gain compared to classical pressurized storage.

5. Conclusion

N_2 and H_2 isotherms measurements performed at 77 K – 1 bar and 298 K – 120 bar on *Sap1.2* and Ni-saponites record low SSAs ranging from 9 to 40 m^2/g and modest H_2 uptakes of ~ 0.03 wt% H_2 at 77 K – 1 bar, and < 0.05 wt% H_2 at 298 K – 120 bar. These low values indicate that Ni functionalization do not create specific crystallographic sites for H_2 adsorption. However, it is observed that H_2 uptake is strongly controlled by external conditions, in particular outgassing temperature that influences the interlayer space opening through its hydration state. Measurements on Ni-pillared saponite highlight that an outgas of 70 °C preserves the interlayer space porosity for H_2 adsorption, in comparison to other saponites routinely outgassed at 150 °C. It is likely that H_2 can only access the inter particles pore space and the basal and lateral adsorption sites in these latter samples outgassed at 150 °C. This is supported by the linear correlation in between SSA and H_2 uptake at 1 bar and 77 K, illustrating that neither N_2 nor H_2 enter porosity inside the structure.

The precursor gel *(Gel_Sap1.2)* used for saponite synthesis, is an exception as it displays an SSA of 145 m^2/g together with a high microporosity and an H_2 uptake of 0.19 wt% at 77 K and 1 bar, and up to 0.12 wt% at 298 K and 120 bar. This latter uptake is equivalent to what can achieve the *MOF-177* under identical conditions.

The comparison of saponite with other clay materials from literature show that precursor gels and high SSA materials are better candidates for H_2 storage, and they should be further investigated for their microporous features and high H_2 uptakes. Indeed, our results tend to illustrate that increasing SSA is a suitable way to enhance H_2 uptake in clay materials, rather than modifying the structure through cations functionalization. Among technical protocols for SSA enhancement, acid treatment is commonly used as it creates new pores despite the destruction of the structure and the apparition of many defects in the case of crystallized materials [32,83].

From a more general perspective, the high density of clay materials may not be a serious issue for many applications where weight is not a matter of concern, such as energy storage for land-based application (power stations or residential areas) or ballasts of the ships. Furthermore, the low cost and widespread availability of clays provide a significant advantage in these cases.

Declaration of competing interest

The authors declare that they have no known competing financial interests or personal relationships that could have appeared to influence the work reported in this paper.

Acknowledgements

This work was financially supported by ORANO industry and the ANR OCCAMH2. The geochemistry-mineralogy platform of ISTerre (Grenoble, France) used for most measurements is partially funded by a grant from Labex OSUG@2020 (investissements d'avenir, ANR10-LABX56″).

References

[1] Ren J, Musyoka NM, Langmi HW, Mathe M, Liao S. Current research trends and perspectives on materials-based hydrogen storage solutions: a critical review. Int J Hydrogen Energy 2017;42:289–311. https://doi.org/10.1016/j.ijhydene.2016.11.195.
[2] Lim KL, Kazemian H, Yaakob Z, Daud WRW. Solid-state materials and methods for hydrogen storage: a critical review. Chem Eng Technol 2010;33:213–26. https://doi.org/10.1002/ceat.200900376.
[3] Barthelemy H, Weber M, Barbier F. Hydrogen storage: recent improvements and industrial perspectives. Int J Hydrogen Energy 2017;42:7254–62. https://doi.org/10.1016/j.ijhydene.2016.03.178.
[4] Züttel A. Hydrogen storage methods. Naturwissenschaften 2004;91:157–72. https://doi.org/10.1007/s00114-004-0516-x.
[5] Jain IP, Lal C, Jain A. Hydrogen storage in Mg: a most promising material. Int J Hydrogen Energy 2010;35:5133–44. https://doi.org/10.1016/j.ijhydene.2009.08.088.
[6] Kaye SS, Dailly A, Yaghi OM, Long JR. Impact of preparation and handling on the hydrogen storage properties of Zn4O(1,4-benzenedicarboxylate)3 (MOF-5). J Am Chem Soc 2007;129:14176–7. https://doi.org/10.1021/ja076877g.
[7] Han D, Jiang FL, Wu MY, Chen L, Chen QH, Hong MC. A non-interpenetrated porous metal-organic framework with high gas-uptake capacity. Chem Commun 2011;47:9861–3. https://doi.org/10.1039/c1cc12858b.
[8] Langmi HW, Walton A, Al-Mamouri MM, Johnson SR, Book D, Speight JD, et al. Hydrogen adsorption in zeolites A, X, Y and RHO. J Alloys Compd 2003;356–357:710–5. https://doi.org/10.1016/S0925-8388(03)00368-2.
[9] Langmi HW, Ren J, North B, Mathe M, Bessarabov D. Hydrogen storage in metal-organic frameworks: a review. Electrochim Acta 2014;128:368–92. https://doi.org/10.1016/j.electacta.2013.10.190.
[10] Ramirez-Cuesta AJ, Mitchell PCH. Hydrogen adsorption in a copper ZSM5 zeolite. An inelastic neutron scattering study. Catal Today 2007;120:368–73. https://doi.org/10.1016/j.cattod.2006.09.024.
[11] Kadono K, Kajiura H, Shiraishi M. Dense hydrogen adsorption on carbon subnanopores at 77 K. Appl Phys Lett 2003;83:3392–4.
[12] Patchkovskii S, Tse JS, Yurchenko SN, Zhechkov L, Heine T, Seifert G. Graphene nanostructures as tunable storage media for molecular hydrogen. Proc Natl Acad Sci U S A 2005;102:10439–44. https://doi.org/10.1073/pnas.0501030102.
[13] Jordá-Beneyto M, Suárez-García F, Lozano-Castelló D, Cazorla-Amorós D, Linares-Solano A. Hydrogen storage on chemically activated carbons and carbon nanomaterials at high pressures. Carbon N Y 2007;45:293–303. https://doi.org/10.1016/j.carbon.2006.09.022.
[14] DeSantis D, Mason JA, James BD, Houchins C, Long JR, Veenstra M. Techno-economic analysis of metal-organic frameworks for hydrogen and natural gas storage. Energy Fuel 2017;31:2024–32. https://doi.org/10.1021/acs.energyfuels.6b02510.
[15] Li J, Corma A, Yu J. Synthesis of new zeolite structure. Chem Soc Rev 2013;44:7112–27. https://doi.org/10.1039/x0xx00000x.
[16] Ding M, Cai X, Jiang HL. Improving MOF stability: approaches and applications. Chem Sci 2019;10:10209–30. https://doi.org/10.1039/c9sc03916c.
[17] Kumar P, Anand B, Tsang YF, Kim KH, Khullar S, Wang B. Regeneration, degradation, and toxicity effect of MOFs: opportunities and challenges. Environ Res 2019;176:108488. https://doi.org/10.1016/j.envres.2019.05.019.

[18] Bhatia SK, Myers AL. Optimum conditions for adsorptive storage. Langmuir 2006; 22:1688–700. https://doi.org/10.1021/la0523816.
[19] Murray HH. Overview - clay mineral applications. Appl Clay Sci 1991;5:379–95. https://doi.org/10.1016/0169-1317(91)90014-Z.
[20] Murray HH. Traditional and new applications for kaolin, smectite, and palygorskite: a general overview. Appl Clay Sci 2000;17:207–21. https://doi.org/10.1016/S0169-1317(00)00016-8.
[21] Zhou C, Tong D, Yu W. Smectite nanomaterials: preparation, properties, and functional applications. Elsevier Inc.; 2019. https://doi.org/10.1016/B978-0-12-814533-3.00007-7.
[22] Edge J. Hydrogen adsorption and dynamics in clay minerals. 2014.
[23] Neumann BS, Sansom KG. The formation of stable sols from laponite, a synthetic hectorite-like clay. Clay Miner 1970;8:389–404.
[24] Cool P, Vansant EF. Preparation and characterization of zirconium pillared laponite and hectorite. Microporous Mater 1996;6:27–36. https://doi.org/10.1016/0927-6513(95)00080-1.
[25] Schaef HT, Loring JS, Glezakou V-A, Miller QRS, Chen J, Owen AT, et al. Competitive sorption of CO2 and H2O in 2:1 layer phyllosilicates. Geochem Cosmochim Acta 2015;161:248–57. https://doi.org/10.1051/0004-6361/202038870.
[26] Yang N, Liu S, Yang X. Molecular simulation of preferential adsorption of CO2 over CH4 in Na-montmorillonite clay material. Appl Surf Sci 2015;356:1262–71. https://doi.org/10.1016/j.apsusc.2015.08.101.
[27] Busch A, Bertier P, Gensterblum Y, Rother G, Spiers CJ, Zhang M, et al. On sorption and swelling of CO2 in clays. Geomech Geophys Geo-Energy Geo-Resources 2016; 2:111–30. https://doi.org/10.1007/s40948-016-0024-4.
[28] Grekov DI, Suzuki-Muresan T, Kalinichev AG, Pré P, Grambow B. Thermodynamic data of adsorption reveal the entry of CH4 and CO2 in smectite clay interlayer. Phys Chem Chem Phys 2020;19. https://doi.org/10.1039/D0CP02135K.
[29] Ziemiański PP, Derkowski A, Szczurowski J, Kozieł M. The structural versus textural control on the methane sorption capacity of clay minerals. Int J Coal Geol 2020;224. https://doi.org/10.1016/j.coal.2020.103483.
[30] Gil A, Trujillano R, Vicente MA, Korili SA. Hydrogen adsorption by microporous materials based on alumina-pillared clays. Int J Hydrogen Energy 2009;34:8611–5. https://doi.org/10.1016/j.ijhydene.2009.08.057.
[31] Erdoğan Alver B. Adsorption studies of hydrogen and ethylene on cation-exchanged bentonite. Clay Miner 2017;52:67–73. https://doi.org/10.1180/claymin.2017.052.1.04.
[32] Erdoğan Alver B. Hydrogen adsorption on natural and sulphuric acid treated sepiolite and bentonite. Int J Hydrogen Energy 2018;43:831–8. https://doi.org/10.1016/j.ijhydene.2017.10.159.
[33] Edge JS, Skipper NT, Fernandez-alonso F, Lovell A, Srinivas G, Bennington SM, et al. Structure and dynamics of molecular hydrogen in the interlayer pores of a swelling 2:1 clay by neutron scattering. J Phys Chem 2014;118:25740–7.
[34] Ziemiański PP, Derkowski A. Structural and textural control of high-pressure hydrogen adsorption on expandable and non- expandable clay minerals in geologic conditions. Int J Hydrogen Energy 2022. https://doi.org/10.1016/j.ijhydene.2022.06.204.
[35] Thomas KM. Adsorption and desorption of hydrogen on metal-organic framework materials for storage applications: comparison with other nanoporous materials. Dalton Trans 2009:1487–505. https://doi.org/10.1039/b815583f.
[36] Voskuilen TG, Pourpoint TL, Dailly AM. Hydrogen adsorption on microporous materials at ambient temperatures and pressures up to 50 MPa. Adsorption 2012; 18:239–49. https://doi.org/10.1007/s10450-012-9397-z.
[37] Ray SS, Okamoto K, Okamoto M. Structure - property relationship in biodegradable poly(butylene succinate)/Layered silicate nanocomposites. Macromolecules 2003: 2355–67.
[38] Claverie M, Garcia J, Prevost T, Brendlé J, Limousy L. Inorganic and hybrid (organic-inorganic) lamellar materials for heavy metals and radionuclides capture in energy wastes management-A review. Materials 2019;12:1–25. https://doi.org/10.3390/ma12091399.
[39] Zhou CH, Zhou Q, Wu QQ, Petit S, Jiang XC, Xia ST, et al. Modification, hybridization and applications of saponite: an overview. Appl Clay Sci 2019;168: 136–54. https://doi.org/10.1016/j.clay.2018.11.002.
[40] Bergaoui L, Lambert JF, Vicente-Rodriguez MA, Michot LJ, Villiéras F. Porosity of synthetic saponites with variable layer charge pillared by Al13 polycations. Langmuir 1995;11:84–7. https://doi.org/10.1021/la00008a001.
[41] Molinard A, Vansant EF. Controlled gas adsorption properties of various pillared clays. Adsorption 1995;1:49–59. https://doi.org/10.1007/BF00704145.
[42] Kloprogge T. Synthesis of smectites and porous pillared clay catalysts: a review. J Porous Mater 1998;5:5–41. https://doi.org/10.1023/A.
[43] Wang K, Yan X, Komarneni S. CO2 adsorption by several types of pillared montmorillonite clays. Appl Petrochemical Res 2018;8:173–7. https://doi.org/10.1007/s13203-018-0206-9.
[44] Carraro P, Elías V, Blanco AG, Sapag K, Moreno S, Oliva M, et al. Synthesis and multi-technique characterization of nickel loaded MCM-41 as potential hydrogen-storage materials. Microporous Mesoporous Mater 2014;191:103–11. https://doi.org/10.1016/j.micromeso.2014.03.005.
[45] Carraro PM, Blanco AAG, Soria FA, Lener G, Sapag K, Eimer GA, et al. Understanding the role of nickel on the hydrogen storage capacity of Ni/MCM-41 materials. Microporous Mesoporous Mater 2016;231:31–9. https://doi.org/10.1016/j.micromeso.2016.05.017.
[46] Forster PM, Eckert J, Heiken BD, Parise JB, Yoon JW, Jhung SH, et al. Adsorption of molecular hydrogen on coordinatively unsaturated Ni(II) sites in a nanoporous hybrid material. J Am Chem Soc 2006;128:16846–50. https://doi.org/10.1021/ja0649217.
[47] Brindley GW, Bish DL, Wan H-M. Compositions, structures, and properties of nickel-containing minerals in the kerolite-pimelite series. Am Mineral 1979;64: 615–25.
[48] Manceau A, Calas G. Heterogeneous distribution of nickel in hydrous silicates from New Caledonia ore deposits. Am Mineral 1985;70:549–58.
[49] Furukawa H, Miller MA, Yaghi OM. Independent verification of the saturation hydrogen uptake in MOF-177 and establishment of a benchmark for hydrogen adsorption in metal-organic frameworks. J Mater Chem 2007;17:3197–204. https://doi.org/10.1039/b703608f.
[50] Li Y, Yang RT. Gas adsorption and storage in metal-organic framework MOF-177. Langmuir 2007;23:12937–44. https://doi.org/10.1021/la702466d.
[51] Zacharia R, Cossement D, Lafi L, Chahine R. Volumetric hydrogen sorption capacity of monoliths prepared by mechanical densification of MOF-177. J Mater Chem 2010;20:2145–51. https://doi.org/10.1039/b922991d.
[52] Anthony JW, Bideaux RA, Bladh KW, Nichols MC. Handbook of mineralogy. 2001.
[53] Schlegel ML, Manceau A, Charlet L, Chateigner D, Hazemann JL. Sorption of metal ions on clay minerals. III. Nucleation and epitaxial growth of Zn phyllosilicate on the edges of hectorite. Geochem Cosmochim Acta 2001;65:4155–70. https://doi.org/10.1016/S0016-7037(01)00700-1.
[54] Dähn R, Scheidegger AM, Manceau A, Schlegel ML, Baeyens B, Bradbury MH, et al. Neoformation of Ni phyllosilicate upon Ni uptake on montmorillonite: a kinetics study by powder and polarized extended X-ray absorption fine structure spectroscopy. Geochem Cosmochim Acta 2002;66:2335–47. https://doi.org/10.1016/S0016-7037(02)00842-6.
[55] Paineau E, Philippe AM, Antonova K, Bihannic I, Davidson P, Dozov I, et al. Liquid-crystalline properties of aqueous suspensions of natural clay nanosheets. Liq Cryst Rev 2014;1:110–26. https://doi.org/10.1080/21680396.2013.842130.
[56] Grim RE. No title. Clay Miner 1968:464.
[57] Hamilton DL, Henderson CMB. The preparation of silicate compositions by a gelling method. Mineral Mag J Mineral Soc 1968;36:832–8.
[58] Robert JL, Beny JM, Della Ventura G, Hardy M. Fluorine in micas: crystal-chemical control of the OH-F distribution between trioctahedral and dioctahedral sites. Eur J Mineral 1993;5:7–18. https://doi.org/10.1127/ejm/5/1/0007.
[59] de Boer JH, Lippens BC, Linsen BG, Broekhoff JCP, van den Heuvel A, Osinga TJ. Thet-curve of multimolecular N2-adsorption. J Colloid Interface Sci 1966;21: 405–14. https://doi.org/10.1016/0095-8522(66)90006-7.
[60] Horcas I, Fernández R, Gómez-Rodríguez JM, Colchero J, Gómez-Herrero J, Baro AM. WSXM: a software for scanning probe microscopy and a tool for nanotechnology. Rev Sci Instrum 2007;78. https://doi.org/10.1063/1.2432410.
[61] Dazas B, Lanson B, Delville A, Robert JL, Komarneni S, Michot LJ, et al. Influence of tetrahedral layer charge on the organization of interlayer water and ions in synthetic Na-saturated smectites. J Phys Chem C 2015;119:4158–72. https://doi.org/10.1021/jp5123322.
[62] Lanson B, Ferrage E, Hubert F, Prêt D, Mareschal L, Turpault MP, et al. Experimental aluminization of vermiculite interlayers: an X-ray diffraction perspective on crystal chemistry and structural mechanisms. Geoderma 2015; 249–250:28–39. https://doi.org/10.1016/j.geoderma.2015.03.005.
[63] Jones RC. X-ray diffraction by randomly oriented line gratings. Acta Crystallogr 1949;2:252–7. https://doi.org/10.1107/s0365110x49000643.
[64] Ferrage E, Lanson B, Sakharov BA, Drits VA. Investigation of smectite hydration properties by modeling experimental X-ray diffraction patterns: Part I. Montmorillonite hydration properties. Am Mineral 2005;90:1358–74. https://doi.org/10.2138/am.2005.1776.
[65] Ferrage E, Kirk CA, Cressey G, Cuadros J. Dehydration of Ca-montmorillonite at the crystal scale. Part I: structure evolution. Am Mineral 2007;92:994–1006. https://doi.org/10.2138/am.2007.2396.
[66] Sun W, Rui X, Ulaganathan M, Madhavi S, Yan Q. Few-layered Ni(OH)2 nanosheets for high-performance supercapacitors. J Power Sources 2015;295:323–8. https://doi.org/10.1016/j.jpowsour.2015.07.024.
[67] Brindley GW, Brown G. Crystal structures of clay minerals and their X-ray identification. Mineralogical Society of Great Britain and Ireland; 1980. https://doi.org/10.1180/mono-5.
[68] Michot LJ, Bihannic I, Pelletier M, Rinnert E, Robert J-L. Hydration and swelling of synthetic Na-saponites: influence of layer charge. Am Mineral 2005;90:166–72. https://doi.org/10.2138/am.2005.1600.
[69] Derkowski A, Kuligiewicz A. Thermal analysis and thermal reactions of smectites: a review of methodology, mechanisms, and kinetics. Clay Clay Miner 2023. https://doi.org/10.1007/s42860-023-00222-y.
[70] Franco F, Prez-Maqueda LA, Pérez-Rodriguez JL. Influence of the particle-size reduction by ultrasound treatment on the dehydroxylation process of kaolinites. J Therm Anal Calorim 2004;78:1043–55. https://doi.org/10.1007/s10973-005-0469-0.
[71] Thommes M, Kaneko K, Neimark AV, Olivier JP, Rodriguez-Reinoso F, Rouquerol J, et al. Physisorption of gases, with special reference to the evaluation of surface area and pore size distribution (IUPAC Technical Report). Pure Appl Chem 2015;87:1051–69. https://doi.org/10.1515/pac-2014-1117.
[72] Jablonska B, Busch M, Kityk AV, Huber P. Natural and chemically modified post-mining clays — structural and surface properties and preliminary tests on copper sorption. Minerals 2019;9:1–20. https://doi.org/10.3390/min9110704.
[73] Jin J, Zheng C, Yang H. Natural diatomite modified as novel hydrogen storage material. Funct Mater Lett 2014;7. https://doi.org/10.1142/S1793604714500271.
[74] Mondelli C, Bardelli F, Vitillo JG, Didier M, Brendle J, Cavicchia DR, et al. Hydrogen adsorption and diffusion in synthetic Na-montmorillonites at high pressures and temperature. Int J Hydrogen Energy 2015;40:2698–709. https://doi.org/10.1016/j.ijhydene.2014.12.038.

[75] Bardelli F, Mondelli C, Didier M, Vitillo JG, Cavicchia DR, Robinet JC, et al. Hydrogen uptake and diffusion in Callovo-Oxfordian clay rock for nuclear waste disposal technology. Appl Geochem 2014;49:168–77. https://doi.org/10.1016/j.apgeochem.2014.06.019.
[76] Sing KSW, Everett DH, Haul RAW, Moscou L, Pierotii RA, Rouquerol J, et al. Reporting physisorption data for gas/solid systems. Int Union Pure Appl Chem 1985;57:603–19. https://doi.org/10.1351/pac198254112201.
[77] Carrado KA, Csencsits R, Thiyagarajan P, Seifert S, Macha SM, Harwood JS. Crystallization and textural porosity of synthetic clay minerals. J Mater Chem 2002;12:3228–37. https://doi.org/10.1039/b204180b.
[78] Horikawa T, Do DD, Nicholson D. Capillary condensation of adsorbates in porous materials. Adv Colloid Interface Sci 2011;169:40–58. https://doi.org/10.1016/j.cis.2011.08.003.
[79] Sarac Oztuna FE, Beyazay T, Unal U. Facile synthesis of graphene aerogel supported nickel/nickel oxide core-shell nanoparticles: efficient electrocatalysts for oxygen evolution reactions. J Phys Chem C 2019;123:28131–41. https://doi.org/10.1021/acs.jpcc.9b07460.
[80] Bastos-Neto M, Patzschke C, Lange M, Möllmer J, Möller A, Fichtner S, et al. Assessment of hydrogen storage by physisorption in porous materials. Energy Environ Sci 2012;5:8294–303. https://doi.org/10.1039/c2ee22037g.
[81] Panella B, Hirscher M, Roth S. Hydrogen adsorption in different carbon nanostructures. Carbon N Y 2005;43:2209–14. https://doi.org/10.1016/j.carbon.2005.03.037.
[82] Suh PM, Park HJ, Prasad TK, Lim D-W. Hydrogen storage in metal-organic frameworks. Chem Rev 2012;112:782–835. https://doi.org/10.1021/cr200274s.
[83] Komadel P. Acid activated clays: materials in continuous demand. Appl Clay Sci 2016;131:84–99. https://doi.org/10.1016/j.clay.2016.05.001.